Critical Condition for Plasma Confinement in the Source of a Magnetic Nozzle Flow

Justin M. Little and Edgar Y. Choueiri

***Abstract*— The existence of a theoretically predicted critical magnetic field strength for efficient plasma confinement in helicon plasma thrusters is verified experimentally in the source of a magnetic nozzle (MN) flow. Control of the plasma confinement is crucial for enhancing the mass utilization efficiency of electric propulsion systems that employ MNs. Langmuir probe measurements of the density at the MN throat of a helicon plasma thruster as a function of the applied magnetic field strength indicate a transition from a low-confinement operation mode, in which a majority of the plasma diffuses to the solid walls of the plasma source before emerging from the thruster, to a high-confinement operation mode, in which the plasma preferentially exhausts downstream through the MN. This transition is shown to be governed by the anisotropic Péclet number, Pe_{an}, which is defined as the ratio of the advective (field aligned) to diffusive (cross field) mass transport rates. Experimental estimations of the mass utilization efficiency of the plasma source for various magnetic field strengths and plasma source lengths are shown to support an analytically derived scaling law, and suggest $Pe_{\mathrm{an}} \gg 1$ as a design criterion for MN plasma sources.**

***Index Terms*— Cross-field diffusion, helicon plasma, magnetic nozzle (MN), radio-frequency (RF) plasma.**

I. Introduction

ELECTRODELESS acceleration of plasma generated by radio-frequency (RF) waves may provide the foundation for a new class of high-efficiency, long-lifetime electric propulsion systems. As an electrothermal thruster, the plasma formed owing to the absorption of RF power into a propellant gas is channeled through a convergent–divergent magnetic field, or magnetic nozzle (MN) [1], [2]. Depending on the system, ion acceleration is achieved through one or a combination of the following mechanisms: ion magnetic moment conservation [3], [4], ambipolar electric fields resulting from electron thermal expansion [5]–[7], and current-free double layers [8]–[11]. Momentum is transferred back to the MN by internal plasma currents [12], [13].

One such device is the helicon plasma thruster (HPT) [14]–[20], which is the commonly used nomenclature for an electrodeless thruster that uses high-frequency RF radiation (typically 13.56 MHz) and plasma source (PS) geometries that favor the propagation of helicon plasma waves [21], [22]. Characteristically, the electron temperature, T_e, is a few orders of magnitude greater than the ion temperature, T_i, in helicon plasmas [22], [23]. Expansion of the hot electrons in the MN results in the formation of an ambipolar electric field that accelerates the ion population to supersonic velocities [6]. The neutral particles remain relatively cold because the electron–neutral collision mean-free path is typically much greater than the scale length of the thruster. Furthermore, except for a few cases [7], [24], the solid surfaces of the thruster are not contoured to efficiently capture the gas dynamic acceleration of the neutral population. Therefore, the thrust contribution of the neutral population in the idealized limit is expected to be much less than that of the ions and electrons, and is often neglected [25].

Direct thrust measurements of HPTs have shown poor performance [16]–[20]. The primary reasons for the poor performance may be understood by considering the separate processes of ionization and acceleration of the propellant gas. The specific impulse, I_{sp}, and thrust efficiency, η, may be written in the following form:

$$I_{\mathrm{sp}} \equiv \frac{F}{\dot{m} g_0} = \eta_m C_T \times \frac{c_s}{g_0} \tag{1}$$

$$\eta \equiv \frac{F^2}{2\dot{m} P_{\mathrm{tot}}} = (\eta_m C_T)^2 \times \left(\frac{\dot{m} c_s^2}{2 P_{\mathrm{tot}}}\right) \tag{2}$$

where F is the thrust, $\dot{m}$ is the propellant mass flow rate, g_0 is the gravitational constant, $c_s = \sqrt{T_e/m_i}$ is the ion-acoustic speed, and P_{tot} is the input power. We assume the ions remain singly charged, and define the mass utilization efficiency as $\eta_m \equiv \dot{m}_i/\dot{m}$, where $\dot{m}_i$ is the ion mass flow rate. The thrust coefficient, C_T, is defined as the ratio of the thrust to the pressure force at the throat of the nozzle [26].

Immediately we notice the importance of both η_m and C_T on the specific impulse and thrust efficiency. A high-performance HPT must therefore both efficiently ionize and accelerate a large percentage of the input propellant. Additionally, the dependence on c_s in (1) represents the well-known scaling of electrothermal thrusters, $I_{\mathrm{sp}} \sim \sqrt{T_e/m_i}$, while the last term in (2) can be viewed as a metric for the efficiency of the PS.

C_T is mainly a function of the radial density profile of the plasma entering the MN and the shape of the MN [12], [26]. η_m depends on the antenna power coupling efficiency, plasma confinement, and collisional processes [25].

Manuscript received December 2, 2013; revised March 14, 2014 and April 23, 2014; accepted April 29, 2014. The work of J. M. Little was supported in part by the Department of Defense through the National Defense Science and Engineering Graduate Fellowship Program and in part by the Program in Plasma Science and Technology through DOE under Contract DE-AC02-09CH11466.

The authors are with the Electric Propulsion and Plasma Dynamics Laboratory, Princeton University, Princeton, NJ 08540 USA (e-mail: jml@princeton.edu; choueiri@princeton.edu).

Color versions of one or more of the figures in this paper are available online at http://ieeexplore.ieee.org.

Digital Object Identifier 10.1109/TPS.2014.2322522

It has been reported that the poor measured performance of HPTs is likely due to low η_m, with values of $\eta_m \sim 0.01$–0.2 inferred from the data [17], [20]. Because $C_T \sim 2$–7 typically [26], it is critical to raise η_m above the values reported in the literature to make HPTs competitive with established thrusters.

Global models of helicon plasmas have been used to estimate the plasma density by equating the absorbed RF power to the power lost by the flux of plasma to the radial walls of the PS, and axially along the applied magnetic field [22], [27]. HPTs require the power to be preferentially lost through the exhaust, thus the mass flux in the radial direction due to cross-field diffusion of the plasma should remain much smaller that the flux due to the field-aligned advection of the plasma.

A detailed 2-D model of an HPT including the PS and MN regions has recently been put forth by Ahedo and Navarro-Cavallé [25]. They analytically solve the two-fluid plasma equations by separating the axial and radial dynamics for plasma confined by an axial magnetic field within a dielectric cylinder that is open at one end. The conditions at the open end of the PS are matched to the numerical MN simulations of Ahedo and Merino [12]. Using this model, they show that η_m increases with the ratio of the length of the PS to the effective mean-free path for collisional ionization. Furthermore, they find a sharp rise in η_m at a critical applied magnetic field strength for a fixed $\dot{m}$ and T_e, which indicates a transition from a low-confinement, low-ionization regime to a high-confinement, high-ionization regime.

Although experiments have generally demonstrated better performance for HPTs with increasing magnetic field values [19], [20], [28], to what extent the performance enhancement is unclear due to improved plasma confinement in the PS (higher η_m) [20], or decreased outward diffusion of the plasma in the MN expansion region (higher C_T) [28]. The goal of this paper is to provide experimental verification of the existence of a critical magnetic field for efficient plasma confinement in MN PSs, find a dimensionless parameter that governs the confinement, and determine how the mass utilization efficiency scales with this parameter.

We provide a detailed description of the experimental setup, including the PS and diagnostics, in Section II. We present the main characteristics of the plasma in our experiment in Section III, with emphasis on the different operating modes of the PS, the influence of the applied magnetic field strength on the density at the MN throat, and the effect of increasing the PS length on the radial structure of the plasma. Finally, in Section IV, we introduce a dimensionless parameter that governs the transition from low-to-high-confinement, analytically derive a scaling law for the mass utilization efficiency in terms of this parameter, and compare this scaling law with experimental measurements.

II. Experimental Setup

The PS (Fig. 1) consists of a 7.5 cm inner diameter, 30.5-cm-long tube of borosilicate glass mounted concentrically inside two electromagnetic coils. The tube is wrapped with grounded copper mesh to prevent stray RF fields outside

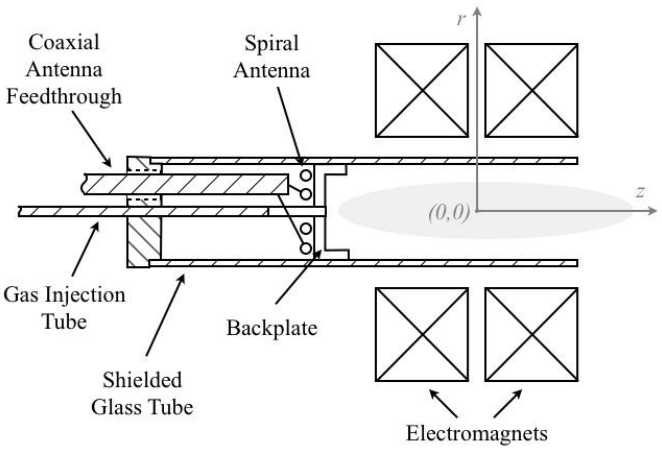

Fig. 1. Schematic of the flat-spiral antenna RF PS.

of the PS [29]. The entire assembly is mounted on a flat plate that is attached to the end of a swinging-arm thrust stand, which will not be used in this paper.

We use a two-turn spiral antenna positioned within the glass tube to excite the plasma. The antenna is not mechanically connected to either the PS or any components on the thrust stand. Using an alumina injection tube, gas is fed through the center of a Macor backplate, which is used to isolate the plasma from the antenna. The backplate has a 5.6 cm inner diameter recession. All of the experiments reported in this paper were conducted using argon as the working gas.

The RF signal is produced by an Agilent 8648B signal generator. An ENI 2100L preamplifier steps the signal up to approximately 20 W, which is fed into an Alpha 9500 linear amplifier capable of producing 1.5 kW. An Alpha 4520 digital wattmeter is used to monitor the standing-wave ratio (SWR) and determine the power delivered to the matching network/antenna (P_D). This system is capable of generating RF power over a range of frequencies, however, we limit our tests to 13.56 MHz.

The power is transferred to the antenna via the L-type impedance matching network that is mounted rigidly inside of the vacuum chamber and mechanically isolated from the thrust stand. The matching network consists of two Comet vacuum-variable capacitors with a range of 5–500 pF. Each capacitor is rated at 5 kV. Depending on the antenna position, the experiment was performed with a reflected power between 4% and 20% of the incident power, with higher reflected powers observed for a longer effective antenna length. Frequency adjustments on the order of 0.01 MHz were sometimes used to obtain a better match [30].

We designed the matching network such that the antenna leads are mounted on two copper rail electrodes that are aligned parallel to the axis of the device to allow adjustment of the axial position of the antenna. Furthermore, the Macor backplate and gas injection tube may be translated axially to remain next to the antenna. This design allows for adjustment of the axial position of the antenna and gas injection location within a 13 cm range.

The electromagnets were made by wrapping 144 turns (12×12) of AWG 10 square, copper magnet wire wound

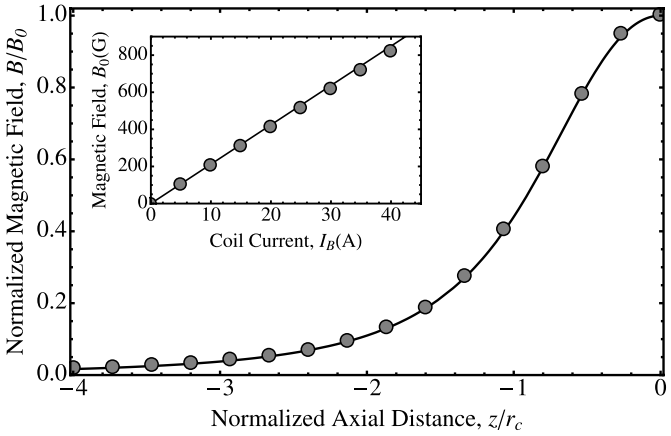

Fig. 2. Axial variation of the magnetic field strength, B, relative to its value at the throat, B_0. Inset: Dependence of B_0 on the magnet current, I_B. Circles: Measured quantities. Black line: Theoretical prediction.

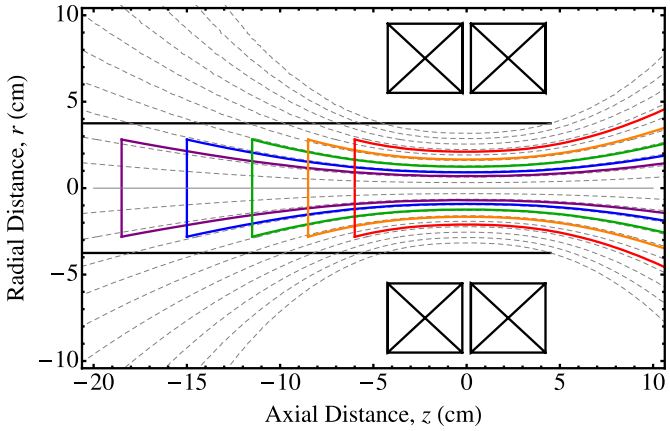

Fig. 3. Magnetic flux contours (dashed) are shown along with the flux contours corresponding to the plane of the following injection locations: $L_{\mathrm{bp}} = 6.0$ cm (red), $L_{\mathrm{bp}} = 8.5$ cm (orange), $L_{\mathrm{bp}} = 11.5$ cm (green), $L_{\mathrm{bp}} = 15.0$ cm (blue), and $L_{\mathrm{bp}} = 18.0$ cm (purple).

around an aluminum mandrel. The effective radius of each coil was measured to be $r_c = 7.51$ cm, which corresponds closely to the physical radius of the center of the copper windings. The magnets are powered using an Amrel SPS32 DC switching power supply, and are each capable of handling up to 50 A of current.

The magnets were designed such that they may move independently with respect to each other and the glass tube, thus allowing control over the physical and magnetic geometries of the PS. A single configuration is used throughout the duration of this experiment (Fig. 1) whereby the magnets are connected rigidly together with an axial separation of 4.5 cm between their effective centers.

Gaussmeter measurements of the relative magnetic field strength along the nozzle axis are shown in Fig. 2. The magnitude of the maximum magnetic field as a function of the coil current, I_B, is also shown in the inset. The solid black lines in Fig. 2 result from approximating the two magnets as single loops of current with radius r_c. Continuing with this approximation, the surfaces of constant magnetic flux are shown in Fig. 3 as dashed lines. The colored lines correspond to the different injection planes and bounding magnetic flux surfaces used throughout the experiment.

Plasma from the open end of the PS is exhausted into the EPPDyL's large dielectric pulsed propulsion (LDPP) vacuum chamber. The cylindrical chamber is made out of fiberglass and measures 8 ft in diameter and 25 ft in length. The chamber is evacuated using two mechanical Stokes roughing pumps, a roots blower, and a 48 in diameter CVC diffusion pump rated at 95 000 l/s of pumping capacity. The facility is also equipped with liquid nitrogen baffles, which are not used in this experiment. Pressure is measured using a Varian ConvectTorr vacuum gauge and Varian 525 cold cathode gauge connected to a Varian L8350 multigauge controller. The vacuum system has a minimum base pressure of 2×10^{-6} torr; however, vacuum leaks are restricted the base pressure of the present experiments to 5×10^{-5} torr. During operation, the tank pressure never exceeded 1×10^{-4} torr.

The primary diagnostic used in this paper is an RF-filtered Langmuir probe (LP) [31]. RF filtering uses four chip inductors: two each with a self-resonant frequency of 14 and 28 MHz. The probe tip is made of tungsten wire and has a 0.25 mm diameter and 1.0 mm length. The wire is friction-fit to a stainless steel tube and inserted in an alumina tube. A 0.1 mm wide by 0.5 mm deep recess exists between the probe tip and alumina jacket so that the tip remains electrically isolated from any conductive coating that could potentially be sputtered onto the jacket. The error in the calculation of the probe tip area is estimated as 15%.

The LP bias voltage is produced by a three-stage phase shift oscillator that drives a Kepco 1000M bipolar operational power/amplifier (BOP) to produce a 5 Hz, 140 V peak-to-peak waveform. The BOP is connected to the LP using BNC cables on each side of a vacuum feedthrough. Current from (to) the probe is measured across the 1 kΩ resistor of a low-pass filter and displayed on a Tektronix TDS 3034B digital oscilloscope.

Typical current–voltage (IV) curves are obtained by averaging over eight waveform periods. The electron temperature is found from the inverse of the slope of the linear region of the $\ln I_e - V$ graph [32]. The error due to this method for our LP is estimated as 25% [31]. It is possible to decrease this error using an additional electrode to act as a reference for the plasma potential, however, this occurs at the cost of added complexity and intrusiveness.

The plasma density, n_i, was found from the ion saturation region of the IV curve [32]. Sheath expansion effects of cylindrical LPs have previously been accounted for in the literature by linear extrapolation of the ion saturation current to either the floating potential, V_f [33], or the plasma potential V_p [34]. We obtain n_i from the average of these two methods, and estimate the error as one-half of the difference between these methods added in quadrature with the electron temperature and probe tip area uncertainties.

The LP is mounted on a small fiberglass rod positioned perpendicular to the thruster axis and located approximately 30 cm from the exit of the PS. The axial location of the LP tip corresponds to the location of maximum applied magnetic field

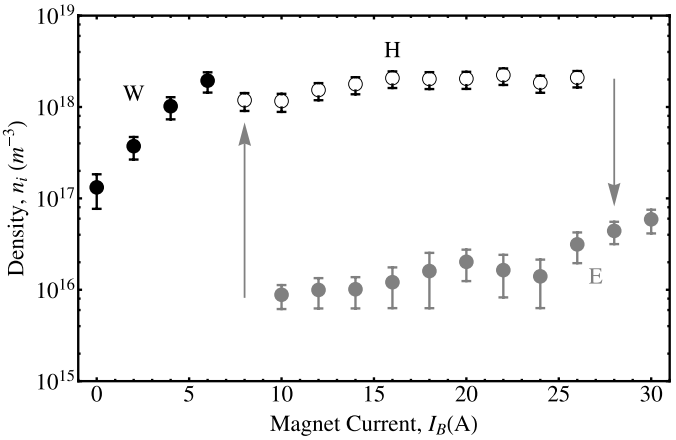

Fig. 4. Langmuir probe measurements of the plasma density at the MN throat, n_i, versus magnet current, I_B, measurements indicate the presence of three distinct modes: wave mode (W), inductive mode (H), and capacitive mode (E). The operating parameters are $P_D = 500$ W, $\dot{m} = 2$ mg/s, and $L_{\text{bp}} = 11.5$ cm. Arrows: Direction of the mode transition to and from the E mode. A similar hysteresis was not observed for the W–H transition. Note that the decreasing density of the W mode at low magnetic fields is due to diffusion of the plasma to the walls prior to reaching the probe [see Fig. 5(b)].

($z = 0$), or MN throat. The radial location is controlled with a single-axis translation stage that is capable of positioning the probe with an accuracy of ∼1 mm.

III. Plasma Characterization

We found the PS to operate in three distinct modes depending on the argon mass flow rate, applied magnetic field strength, injection location, and RF power. For convenience sake, we refer to these modes according to the commonly observed modes in RF plasmas [27]: the capacitive mode (E), inductive mode (H), and helicon wave mode (W). We will show that the characteristics of each mode agree qualitatively with those observed in the literature; however, we emphasize the fact that we did not make wave measurements to discern the E, H, and W modes [35].

The discharge was most commonly ignited in the E mode, which was distinguished by a faint glow with electron temperatures and ion densities on the order $T_e \sim 10$ eV and $n_i \sim 10^{16}$–10^{17} m^{-3}. For fixed P_D and $\dot{m}$, as we decreased the magnetic field below a certain threshold the plasma would jump into either the H or W mode, leading to an impedance mismatch that had to be corrected using the tuning capacitors. The plasma was observed to be much brighter in the W mode and demonstrated the blue core characteristic of Helicon plasmas reported in the literature [21]. The temperature and density of the W mode were measured to be $T_e \sim 5$ eV and $n_i \sim 10^{18}$–10^{19} m^{-3}, respectively. Finally, we observed a second impedance mismatch while increasing the magnetic field, which suggests a W–H mode transition. The H mode was slightly less bright than the W mode and did not possess a blue core. We observed T_e to be comparable between the W and H modes, while n_i showed a slight decrease upon transitioning from the W to H mode.

We note that the density in the W mode appears lower than that of the H mode at low magnetic fields as shown in Fig. 4 due to diffusion of the plasma to the PS walls prior to reaching the LP. Indeed, LP measurements near the backplate reveal that the W mode densities remain a few times larger than the H mode densities in this region, which is consistent with previous studies of helicon PSs [21], [36].

Within a given mode, T_e increased slightly as $\dot{m}$ decreased, which agrees with previous theoretical [27] and experimental results [37]. The inverse relationship between T_e and B_0, predicted to be a consequence of improved confinement of the plasma [38], [39], was not observed in our experiment. Rather, we found T_e to be insensitive to changes in B_0 within our experimental uncertainty. We anticipate that this discrepancy may be due to the open-ended nature of our device. T_e is typically determined by the balance between ionization and particle losses within the PS [27]. In the limit that the loss of particles due to advection along the magnetic field dominates diffusive losses to the PS walls, the particle balance (and therefore T_e) becomes intensive to changes in B_0.

Helicon modes in low-magnetic-field RF plasmas have previously been observed in the literature [40], [41], and have been recently studied in depth by Lafleur *et al.* [42]–[45]. A few curious distinctions between the mode transitions observed in our PS (using a spiral antenna) and those found in literature (typically with a Boswell-type antenna) are worth mentioning: 1) the W mode existed for applied magnetic fields that are an order of magnitude larger than previously observed; and 2) the density jump between E and W modes was around two orders of magnitude, compared with less than an order of magnitude reported in the literature.

Although it appears that the W mode in our experiment was stable at $B_0 = 0$ G, theory indicates that the propagation of helicon waves requires a finite background magnetic field [27]. Therefore, it is possible that a second inductive mode exists at $B_0 = 0$ G [46].

For the remainder of this paper, we operated the PS in the W and H modes at a fixed delivered power, $P_D = 500$ W, and argon mass flow rate, $\dot{m} = 2$ mg/s. We performed experiments for five different backplate locations, which correspond to the following magnetic flux contour colors as shown in Fig. 2: $L_{\text{bp}} = 6.0$ cm (Red), $L_{\text{bp}} = 8.5$ cm (Orange), $L_{\text{bp}} = 11.5$ cm (Green), $L_{\text{bp}} = 15.0$ cm (Blue), and $L_{\text{bp}} = 18.0$ cm (Purple). Here, $L_{\text{bp}} = |z_{\text{bp}}|$.

Photographs of the PS operating at various applied magnetic field strengths for $L_{\text{bp}} = 11.5$ cm are shown in Fig. 5. At zero applied magnetic field, much of the plasma remained inside the glass tube of the PS. As we increased the magnetic field, the plasma migrated downstream and eventually formed a plume in the MN divergent field. This behavior indicates that, without a magnetic field, the majority of plasma is lost to the glass walls through diffusion. Increasing the applied magnetic field decreases the radial diffusion of the plasma, allowing the plasma to advect through the glass tube opening to form a plume. We verified this notion using thermal infrared camera measurements, which showed that the rate of heating of the glass tube near the injection location decreased inversely with the magnetic field strength.

Also shown in Fig. 5 are the approximate magnetic flux surfaces that intersect the glass tube at the exhaust, ψ_w, and

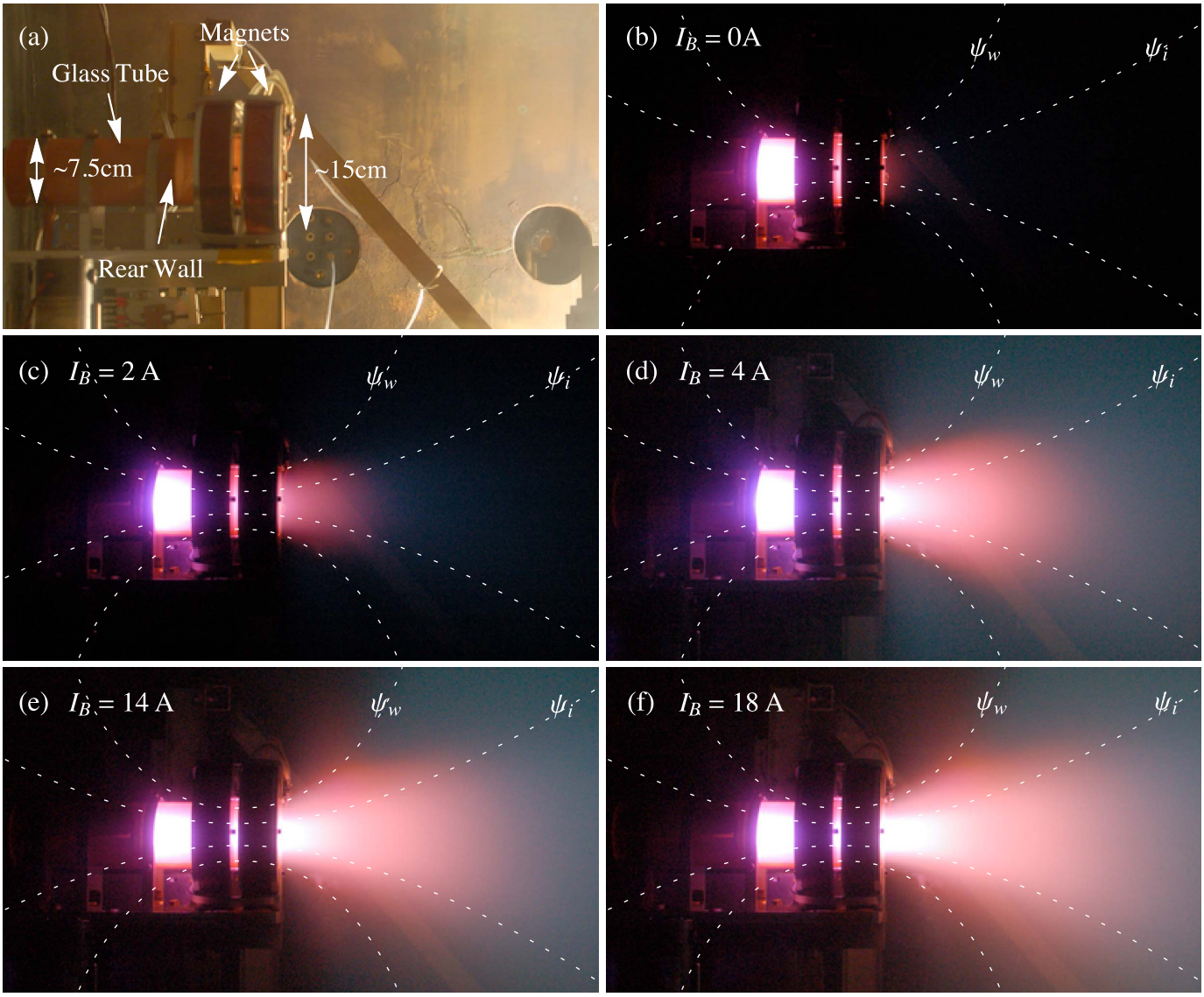

Fig. 5. Photographs (f/7.1, 1/30 s exposure) of the (a) PS operating at (b)–(f) various magnet currents, I_B. The operating parameters are $P_D = 500$ W, $\dot{m} = 2$ mg/s, and $L_{\text{bp}} = 11.5$ cm [note that the backplate location shown in (a) corresponds to $L_{\text{bp}} = 8.5$ cm]. (b)–(d) Photos depicting the blue core of the helicon mode, which is absent from the (e)–(f) inductive mode. Dashed white lines: Surfaces of constant magnetic flux corresponding the surfaces that intersect the glass tube at the exhaust, ψ_{t_0}, and the inner radius of the backplate recession at the injection plane, ψ_i.

the inner radius of the backplate at the injection plane, ψ_i. Fig. 5(c)–(f) shows that the edge of the bright plasma core corresponded roughly to ψ_i. Furthermore, as we increased I_B, the boundary of this core became even sharper, especially in the plume.

We also looked at the effect of moving the backplate on the plasma structure. The intersecting flux surface (ψ_i) compresses radially as the backplate is moved upstream (see Fig. 3). This explains the radial compression observed of the advective core, as seen in the photographs in Fig. 6. It is clear from these pictures that, as the core was compressed, the divergence of the plume decreased dramatically: a result that qualitatively agrees with MN performance models [12], [26], and suggests higher performance for larger L_{bp}.

Using the LP, we measured the plasma density and electron temperature at the MN throat as a function of the applied magnetic field. The results for four different backplate locations are shown in Fig. 7. Here, the colors of the data points correspond to the colored contours shown in Fig. 3. Furthermore, the solid data points denote W mode plasmas, while the open data points denote H mode plasmas. The W–H mode transition was assumed to occur when both the impedance match and visible emission changed abruptly as described earlier in this section. We note that the shaded region shown in Fig. 7 corresponds to an I_B-range in which the plasma was unable to remain impedance matched at $P_D = 500$ W.

In general, the plasma density at the MN throat increased with the applied magnetic field in the W mode. As I_B increased beyond a certain threshold, the plasma transitioned to the H mode and was marked by a slight decrease in n_i for both $L_{\text{bp}} = 8.5$ cm and $L_{\text{bp}} = 11.5$ cm. We suspect that this decrease indicates diminished power coupling between the

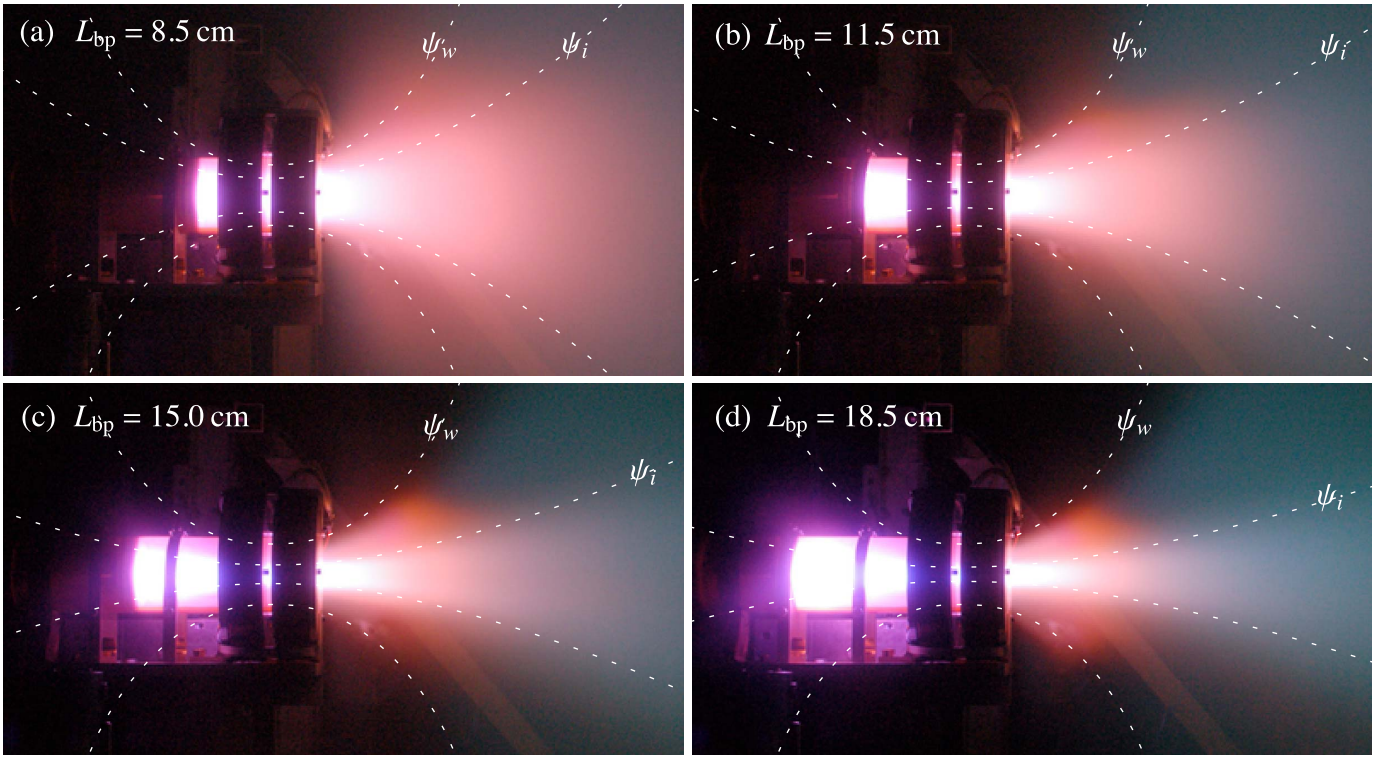

Fig. 6. Photographs (f/7.1, 1/30 s exposure) of the PS operating with (a)–(d) different injection locations, L_{bp}. The operating parameters are $P_D = 500$ W, $\dot{m} = 2$ mg/s. Dashed white lines: Surfaces of constant magnetic flux corresponding the wall radius at the exhaust, ψ_w, and the radius of the backplate recession at the injection plane, ψ_i.

antenna and plasma [27]. We observed neither a W–H nor a H–C mode transition for $L_{bp} = 18.5$ cm in the magnet current range considered, $I_B \leq 32$ A.

The plasma density as $I_B \to 0$ decreased drastically (by nearly three orders of magnitude) as the distance between the injection plane and throat increased. This trend supports the notion that plasma was being lost to the walls through radial diffusion prior to reaching to probe, which was located at a distance L_{bp} from the injection region. Furthermore, we found a sharp rise in n_i with the increasing magnetic field, which is indicative of the low-confinement to high-confinement transition observed analytically by Ahedo and Navarro-Cavallé [25].

We also measured the radial dependence of the plasma density at the MN throat. These results are shown in Fig. 8(a) for various L_{bp}. The radial location of each measurement is normalized by the radius of the PS wall, r_w, and the densities are normalized by $\bar{n}_a$, which will be defined later. In general, the plasma density remained uniform near the axis of the PS to a certain radial distance, after which the density fell off exponentially.

The visible structure of the plasma and radial density measurements support the following scenario: plasma formed in the injection region ($z = -L_{bp}$) with a radially uniform density profile advects along the converging magnetic field toward the throat plane ($z = 0$). The density profile at the throat remains uniform in the limit that transport is governed purely by advection along the magnetic field. However, the plasma density spreads out radially due to cross-field diffusion. We infer the radial uniformity of the density profile at the injection region from the LP probe measurements, which became increasingly more uniform as L_{bp} decreased (i.e., the probe moved closer to the injection region). Furthermore, the exponential radial dependence of the plasma density in the diffusive region is expected from the diffusion equation [47].

Guided by this physical picture, we found the following model to be appropriate to describe the plasma density profile at the MN throat:

$$n_i(r) = \begin{cases} \bar{n}_a & : r < r_a \\ \bar{n}_a \exp[-(r - r_a)/\delta] & : r > r_a \end{cases} \tag{3}$$

where r_a is the boundary between the advective ($r < r_a$) and diffusive ($r > r_a$) regions of the plasma, $\bar{n}_a$ is the average plasma density in the advective region, and δ is the diffusive length scale. The solid lines in Fig. 8(a) represent a least-squares fit of (3) to the radial LP data.

It is seen from Fig. 8(a) that r_a increased inversely with L_{bp}. In the limit of zero cross-field diffusion, the radius of the plasma at $z = 0$ is expected to scale according to

$$r_a \approx r_i / \sqrt{\Pi_B} \tag{4}$$

where we have assumed $B_z \gg B_r$. Here, r_i is the radius of the injection region and $\Pi_B = B_0/B_i$ is the magnetic mirror ratio between the MN throat and injection region.

We compare in Fig. 8(b) the values of r_a found from a least-squares fit of (3) to the radial LP data to the theoretical prediction of (4). Here, we normalize r_a by the radius of the PS wall, r_w. The agreement between the calculated and predicted

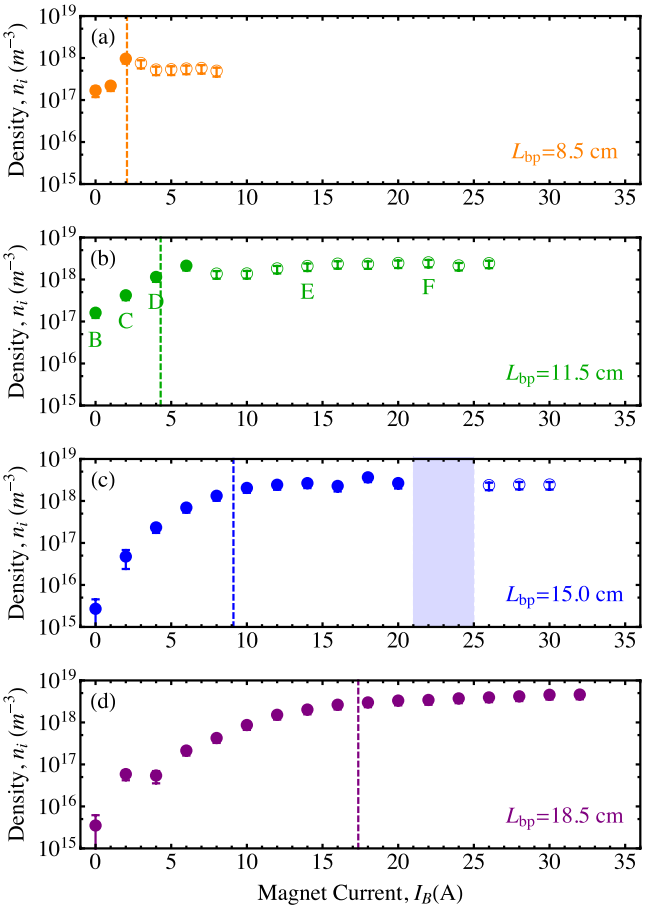

Fig. 7. Langmuir probe density measurements at the center of the MN throat for $P_D = 500$ W, $\dot{m} = 2$ mg/s, and (a)–(d) different injection locations, L_{bp}. The solid and open data points correspond to the W and H modes, respectively. The plasma was not stable at $P_D = 500$ W in the shaded blue region for $L_{bp} = 15.0$ cm. The letters next to the data points in (b) represent the photographs shown in Fig. 5. Dashed vertical lines: Magnet current required to generate the characteristic magnetic field described in Section IV.

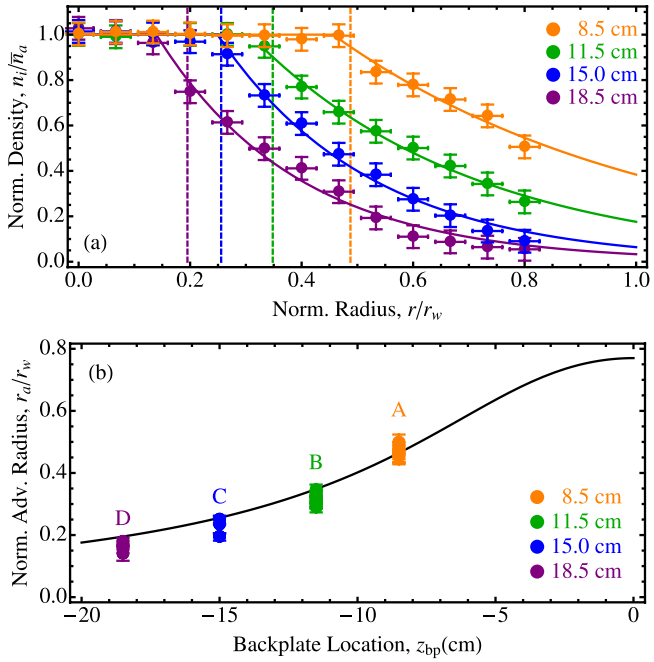

Fig. 8. Radial Langmuir probe measurements of the (a) radial plasma density profile and (b) scaling of the radius of the boundary between the advective and diffusive regions normalized by the wall radius, r_a/r_w. Solid lines in (a) come from (3). Dashed lines: Location of r_a/r_w predicted from (4). Solid line in (b) comes from (4). Note that the letters in (b) correspond to the photographs in Fig. 6.

values of r_a agrees well with the qualitative observations drawn from the photographs shown in Fig. 6.

We take a moment to explain a contradiction between the radial density profiles measured in our experiment and the Bessel function density profile commonly used in MN performance models [12], [26]. The Bessel function profile was adopted from the work of Ahedo [48], who showed that the radial density profile of an infinitely long cylinder of plasma was given by the zeroth-order Bessel function for both unmagnetized plasmas and magnetized plasmas in the large Hall parameter limit. We suspect that the finite length of our PS prevents the emergence of the Bessel function profile for all but the lowest applied magnetic fields. In fact, for magnetic fields below a critical value (see Section IV), we found that the radial density profile was indeed more appropriately described by a Bessel function than the model presented in (3).

Finally, it is necessary to examine the role of azimuthal currents in the transfer of momentum [12], [13] from the plasma to the MN for the density profiles shown in Fig. 8(a). The density plateau near the axis implies that azimuthal currents are negligible within the advective core of the plasma. Therefore, we anticipate that momentum is transferred by the azimuthal current density created by the pressure gradient within the diffusive layer [12], [49]. The fact that the diffusive layer transfers momentum does not imply that the advective core of the plasma does not produce thrust. Rather, the strength of the azimuthal current density in the diffusive layer is proportional to the local plasma density, which is globally influenced by the expansion of both the advective and diffusive regions of the plasma [12].

IV. Critical Condition for Plasma Confinement

The relative importance of field-aligned advection with respect to cross-field diffusion may be analyzed using a dimensionless, anisotropic Péclet number, which we define as

$$Pe_{an} \equiv \frac{c_s/L}{D_\perp/R^2} \tag{5}$$

where c_s is the ion acoustic speed, L is the PS length, R is the PS radius, and $D_\perp$ is the cross-field diffusion coefficient. Effectively, Pe_{an} is the ratio of the cross-field diffusion timescale to the field-aligned advection timescale.

We can use the LP measurements shown in Fig. 7 to relate Pe_{an} to the critical magnetic field predicted by Ahedo and Navarro-Cavallé [25]. The cross-field diffusion coefficient can be written as $D_\perp = \eta_\perp p_e/B^2$ [22]. Here, $p_e = n_e T_e$ is the electron pressure and $\eta_\perp \approx (100 T_{ev})^{-3/2} [\Omega \cdot \text{m}]$ is the cross-field resistivity of the plasma assuming singly charged ions [47]. We can express the anisotropic Péclet number in the

injection region as $Pe_{\text{an}}^{i} = (B_0/B^*)^2$, where

$$B^* \equiv \frac{\Pi_B}{R}\sqrt{\frac{p_e L \eta_\perp}{c_s}} \tag{6}$$

is a characteristic magnetic field. We consider the injection region because it represents the location of minimum Pe_{an} for our convergent-field MN geometry.

Setting $R = r_w$, $L = L_{\text{bp}}$, $n_e = 2 \times 10^{18}$ m^{-3} and $T_{\text{ev}} = 5$ eV in (6) we can calculate the characteristic magnetic field for the data in Fig. 7. As shown in Fig. 2, the magnet current corresponding to B^* for our experiment is approximately $I_B^*[\text{A}] \approx B^*[\text{G}]/21$. The value of I_B^* is shown for different values of L_{bp} in Fig. 7 using a colored dashed line. From this figure we see that B^* corresponds to the magnetic field near which the elbow in the density measurements occur. In other words, B^* represents the critical magnetic field predicted in [25], which suggests that the transition from a low-confinement regime to a high-confinement regime occurs as the magnetic field increases to the point when $Pe_{\text{an}} \sim 1$ in the injection region.

It is clear that plasma confinement within the source region influences the performance of an MN. As a result, the mass utilization efficiency, η_m, should depend strongly upon Pe_{an}. It is important to understand this relationship, thus we seek a simple scaling law between η_m and Pe_{an}. To this end, we adopt and extend in an approximate manner the analytical model of Fruchtman [50].

We consider a cylindrical PS of radius R and length L with a uniform magnetic field directed along the axis of symmetry. We assume that some ionization occurs upstream in a region much smaller than L, which produces an initial ion mass flow rate denoted by $\dot{m}_{i,0}$. For simplicity, we ignore the axial forces on the plasma, and assume the ions flow through the PS at the ion acoustic speed, c_s.

In Fruchtman's model [50], particle balance along the length of the PS is governed by collisional ionization and charge exchange processes. Furthermore, a population of fast ions is created during charge exchange collisions, which are assumed to leave the PS before undergoing further collisions. We extend this model by introducing a term that accounts for the flux of ions to the radial PS walls, which acts as an addition source of fast neutrals.

The 1-D mass conservation equations may be written as

$$\frac{d\dot{m}_i}{dz} = -m_i \Gamma_w + \dot{m}_s/L_{\text{ion}} \tag{7}$$

$$\frac{d\dot{m}_s}{dz} = -\dot{m}_s(1/L_{\text{ion}} + 1/L_{\text{cex}}) \tag{8}$$

$$\frac{d\dot{m}_f}{dz} = m_i \Gamma_w + \dot{m}_s/L_{\text{cex}} \tag{9}$$

where $\dot{m}_i$, $\dot{m}_s$ and $\dot{m}_f$ are the mass flow rates of the ions, slow neutrals, and fast neutrals, respectively, and are subject to the constrain $\dot{m} = \dot{m}_i + \dot{m}_s + \dot{m}_f$.

Additionally, Γ_w represents the ion flux to the wall, and $L_{\text{ion}} \equiv v_s/n_i R_{\text{ion}}$ and $L_{\text{cex}} \equiv v_s/n_i R_{\text{cex}}$ are the effective mean-free path for ionization and charge exchange collisions, respectively. Here, n_i is the ion density, v_s is the speed of the slow neutrals, R_{ion} is the ionization rate, and R_{cex} is the charge–exchange collision rate.

The ion flux to the wall may be written as $\Gamma_w = h_w D_\perp n_{i,r=0}$, where $n_{i,r=0}$ is the ion density along the axis [48]. We note that h_w depends on the shape of the radial density profile, and is constant along z if the density profile remains self-similar. We rewrite $n_{i,r=0}$ in terms of the local ion mass flow rate, $n_{i,r=0} = \dot{m}_i/(h_n m_i c_s A)$. Here, $f_n = n/n_{i,r=0}$ and $h_n = \int f_n dA/A$ are the normalized density profile and its cross-sectional average, respectively.

The first term on the right-hand side of (7) and (9) may then be written as

$$m_i \Gamma_w = \frac{\dot{m}_i}{L}(b/Pe_{\text{an}}) \tag{10}$$

where $b = h_w/(\pi h_n)$ is a constant depending only on f_n.

To gain insight into the fundamental physics governing the PS performance, we simplify the problem by seeking a solution for (7)–(9) assuming that L_{ion}, L_{cex}, and Pe_{an} remain constant throughout the flow. We further assume self-similarity of the density profile, or $df_n/dz = 0$. The solution to (7)–(9) under these assumptions yields

$$\eta_m = \left[\frac{1 + \eta_{m,0}(\Pi - \Psi)}{1 + \Pi - \Psi}\right] e^{-\Psi L^*} - \left(\frac{1 - \eta_{m,0}}{1 + \Pi - \Psi}\right) e^{-(1+\Pi)L^*} \tag{11}$$

where $\eta_{m,0} = \dot{m}_{i,0}/\dot{m}$ and $\eta_m = \dot{m}_{i,L}/\dot{m}$ are the mass utilization efficiency at the PS entrance and exit, respectively.

The solution in (11) is governed by the following dimensionless parameters: $L^* \equiv L/L_{\text{ion}}$, $\Pi \equiv L_{\text{ion}}/L_{\text{cex}}$, and $\Psi \equiv (b/Pe_{\text{an}})/L^*$. A value of $L^* \gg 1$ is desirable to ensure that ionization occurs on a length scale much shorter than the length of the PS [25]. Π is the ratio of the rate at which slow neutrals are lost to charge–exchange in the rate at which they are lost to ionization [50], with $\Pi \ll 1$ required for high η_m. Finally, $\Psi \ll 1$ ensures that the ion wall loss rate remains small compared with the ionization rate.

The exponential dependence on Pe_{an} and L^* in (11) reflect in a generalized form in the observation by Ahedo and Navarro-Cavallé on the existence of a minimum value of B_0 and $\dot{m}$ required to transition to high η_m ([25], Fig. 8). Furthermore, we find that $\eta_m = 1 - e^{-L^*}$ in the limit $\Psi \gg 1$, $\Pi \ll 1$, and $\eta_{m,0} \ll 1$, which, for $L^* > 1.5$, is a good approximation for the implicit relation between η_m and L^* derived by Ahedo and Navarro-Cavallé.

A simple scaling relation between η_m and Pe_{an} emerges if we consider the limit $L^* \gg 1$ and $\Psi \ll 1$, which is valid over most operating conditions of our PS. Equation (11) then becomes

$$\eta_m \approx \left(\frac{1 + \eta_{m,0}\Pi}{1 + \Pi}\right) e^{-b/Pe_{\text{an}}}. \tag{12}$$

Again, the exponential dependence on Pe_{an} emphasizes the importance of proper plasma confinement in the PS. Indeed, it is clear that $\eta_m \to 0$ for $Pe_{\text{an}} \ll 1$. For $Pe_{\text{an}} \gg 1$, however, the plasma is well confined and $\eta_m \to \eta_{\text{hc}}$, where η_{hc} is the mass utilization efficiency at high confinement. We note that η_{hc} depends on both the efficiency of the ionization region,

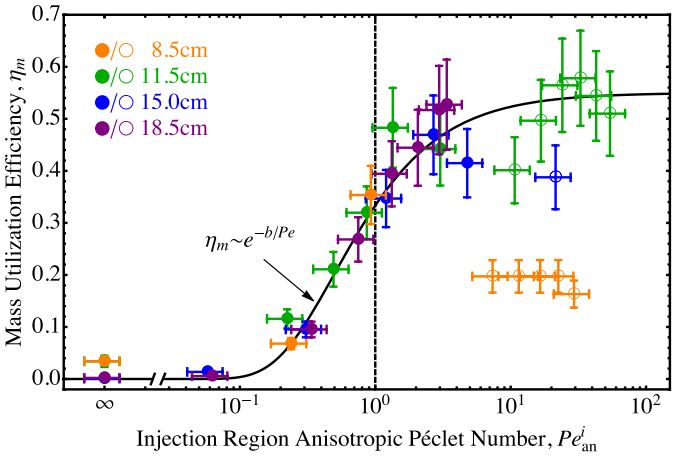

Fig. 9. Scaling of the estimated mass utilization efficiency, η_m, with the injection region anisotropic Péclet number, Pe^i_{an}, for $P_D = 500$ W and $\dot{m} = 2$ mg/s. The solid and open data points correspond to the W and H modes, respectively. Solid black line: (12) with $\eta_{hc} = 0.55$ and $b = 0.5$ chosen for the best fit. The transition between diffusive and advective modes is marked with a dashed line at $Pe^i_{an} = 1$.

$\eta_{m,0}$, and balance between ionization and charge exchange collisions, Π.

We can examine the scaling of η_m with Pe^i_{an} from our experimental data by estimating the mass utilization efficiency as $\eta_m \approx \bar{n}_a m_i A_{eff} c_s / \dot{m}$, where A_{eff} is the effective cross-sectional area that results from integrating the density profile of (3) over the cross-sectional area of the throat plane. We have assumed the ions remain singly charged and satisfy the sonic condition at the MN throat [1].

We show in Fig. 9 the experimentally estimated mass utilization efficiency, η_m, versus the anisotropic Péclet number calculated at the injection plane, Pe^i_{an}. Data is shown for the four backplate locations that correspond to the LP data shown in Figs. 7 and 8. Also shown is a solid line that represent the scaling of η_m with Pe_{an} that we derived in (12). The data clearly shows the transition between a low-confinement and high-confinement mode near $Pe^i_{an} = 1$ (dashed, vertical line). Furthermore, the scaling law derived in (12) appropriately describes this transition.

The mass utilization efficiency measured in the high-confinement limit, $\eta_{hc} \approx 0.55$, implies that $\eta_{m,0} \approx 0.17$. Here, we have used $T_e \approx 5$ eV to calculate $\Pi \approx 1.2$ using the approximate forms for R_{ion} and R_{cex} given by Fruchtman [50]. Measurements at different mass flow rates and powers indicate that η_{hc} increases with P and inversely with $\dot{m}$. For example, we measured $\eta_{hc} \approx 0.75$ for $\dot{m} = 2$ mg/s and $P = 700$ W, and $\eta_{hc} \approx 0.85$ for $\dot{m} = 1$ mg/s and $P = 700$ W. This suggests that the operational regime studied in this paper ($\dot{m} = 2$ mg/s and $P = 500$ W) is power-limited near the ionization region of the antenna. In other words, $\eta_{m,0}$ increases as P increases. Additionally, the inverse relationship between T_e and $\dot{m}$ lowers the value of Π, thus increasing η_{hc}. Thus, while the data in Fig. 9 show a relatively low η_{hc}, the ability to increase η_{hc} by varying $\dot{m}$ and P is encouraging from a propulsion standpoint. Optimization of η_{hc} is a complex problem that requires deeper understanding of the antenna–plasma coupling, and is a topic that merits further investigation.

Finally, we note that the H mode data does not match the predicted scaling as well as the W mode data owing to the decrease in density that occurs during the W–H mode transition, which is especially true for the case of $L_{bp} = 8.5$ cm. We suspect that this is the result of diminished power coupling between the antenna and plasma as evidenced by the impedance mismatch observed during this transition. The scaling for the H mode may be recovered by introducing a different value for $\eta_{m,0}$ that is less than that of the W mode, which is consistent with the lower ionization fractions observed for H mode plasmas [27].

V. Conclusion

We have experimentally verified the analytical prediction by Ahedo and Navarro-Cavallé [25] of the existence of a critical magnetic field above which high-confinement operation of an HPT is achieved. Furthermore, we showed that this transition occurs as the anisotropic Péclet number of the flow, Pe_{an}, increases above unity, where Pe_{an} was defined as the ratio of field-aligned advective to cross-field diffusive transport rates. This transition suggests a new design criteria for HPTs, namely $Pe_{an} \gg 1$. Experimental estimations of the mass utilization efficiency for various magnetic fields and backplate locations support this argument.

Acknowledgment

The authors would like to thank B. Sorenson for valuable assistance with the matching network, RF system, and PS, and Prof. S. Cohen for insightful discussions.

References

[1] S. A. Andersen, V. O. Jensen, P. Nielsen, and N. D'Angelo, "Continuous supersonic plasma wind tunnel," *Phys. Fluids*, vol. 12, no. 3, p. 557, 1969.
[2] K. Kuriki and O. Okada, "Experimental study of a plasma flow in a magnetic nozzle," *Phys. Fluids*, vol. 13, no. 9, p. 2262, 1970.
[3] R. H. Comfort, "The magnetic mirror force in plasma fluid models," *Geophys. Monograph Ser.*, vol. 44, pp. 51–53, Jan. 1988.
[4] B. W. Longmier *et al.*, "VX-200 magnetoplasma thruster performance results exceeding fifty-percent thruster efficiency," *J. Propuls. Power*, vol. 27, no. 4, pp. 915–920, Jul./Aug. 2011.
[5] A. V. Arefiev and B. N. Breizman, "Ambipolar acceleration of ions in a magnetic nozzle," *Phys. Plasmas*, vol. 15, no. 4, p. 042109, Apr. 2008.
[6] B. Longmier *et al.*, "Ambipolar ion acceleration in an expanding magnetic nozzle," *Plasma Sources Sci. Technol.*, vol. 20, no. 1, p. 015007, Jan. 2011.
[7] C. Charles, R. W. Boswell, and K. Takahashi, "Boltzmann expansion in a radiofrequency conical helicon thruster operating in xenon and argon," *Appl. Phys. Lett.*, vol. 102, no. 22, pp. 223510-1–223510-4, Jun. 2013.
[8] C. Charles and R. W. Boswell, "Current-free double-layer formation in a high-density helicon discharge," *Appl. Phys. Lett.*, vol. 82, no. 9, p. 1356, Feb. 2003.
[9] A. Fruchtman, "Electric field in a double layer and the imparted momentum," *Phys. Rev. Lett.*, vol. 96, no. 6, p. 065002, Feb. 2006.
[10] E. Ahedo, "Double-layer formation and propulsive assessment for a three-species plasma expanding in a magnetic nozzle," *Phys. Plasmas*, vol. 18, no. 3, p. 033510, Mar. 2011.
[11] M. Merino and E. Ahedo, "Two-dimensional quasi-double-layers in two-electron-temperature, current-free plasmas," *Phys. Plasmas*, vol. 20, no. 2, p. 023502, Feb. 2013.
[12] E. Ahedo and M. Merino, "Two-dimensional supersonic plasma acceleration in a magnetic nozzle," *Phys. Plasmas*, vol. 17, no. 7, p. 073501, Jul. 2010.

[13] K. Takahashi, T. Lafleur, C. Charles, P. Alexander, and R. W. Boswell, "Electron diamagnetic effect on axial force in an expanding plasma: Experiments and theory," *Phys. Rev. Lett.*, vol. 107, no. 23, p. 235001, Nov. 2011.

[14] R. Winglee, T. Ziemba, L. Giersch, J. Prager, J. Carscadden, and B. R. Roberson, "Simulation and laboratory validation of magnetic nozzle effects for the high power helicon thruster," *Phys. Plasmas*, vol. 14, no. 6, p. 063501, Jun. 2007.

[15] O. V. Batishchev, "Minihelicon plasma thruster," *IEEE Trans. Plasma Sci.*, vol. 37, no. 8, pp. 1563–1571, Aug. 2009.

[16] J. Ling, M. D. West, T. Lafleur, C. Charles, and R. W. Boswell, "Thrust measurements in a low-magnetic field high-density mode in the helicon double layer thruster," *J. Phys. D, Appl. Phys.*, vol. 43, no. 30, p. 305203, Jul. 2010.

[17] S. Pottinger, V. Lappas, C. Charles, and R. W. Boswell, "Performance characterization of a helicon double layer thruster using direct thrust measurements," *J. Phys. D, Appl. Physics*, vol. 44, no. 23, p. 235201, May 2011.

[18] K. Takahashi *et al.*, "Direct thrust measurement of a permanent magnet helicon double layer thruster," *Appl. Phys. Lett.*, vol. 98, no. 14, p. 141503, Apr. 2011.

[19] L. T. Williams and M. L. R. Walker, "Thrust measurements of a radio frequency plasma source," *J. Propuls. Power*, vol. 29, no. 3, pp. 520–527, 2013.

[20] A. Shabshelowitz and A. D. Gallimore, "Performance and probe measurements of a radio-frequency plasma thruster," *J. Propuls. Power*, vol. 29, no. 4, pp. 919–929, 2013.

[21] R. W. Boswell, "Very efficient plasma generation by whistler waves near the lower hybrid frequency," *Plasma Phys. Control Fusion*, vol. 26, no. 10, p. 1147, Oct. 1984.

[22] F. F. Chen, "Experiments on helicon plasma sources," *J. Vac. Sci. Technol. A, Vac., Surf., Films*, vol. 10, no. 4, pp. 1389–1401, Jul. 1992.

[23] J. L. Kline, E. E. Scime, R. F. Boivin, A. M. Keesee, X. Sun, and V. S. Mikhailenko, "RF absorption and ion heating in helicon sources," *Phys. Rev. Lett.*, vol. 88, no. 19, p. 195002, Apr. 2002.

[24] C. Charles, K. Takahashi, and R. Boswell, "Axial force imparted by a conical radiofrequency magneto-plasma thruster," *Appl. Phys. Lett.*, vol. 100, no. 11, p. 113504, Mar. 2012.

[25] E. Ahedo and J. Navarro-Cavallé, "Helicon thruster plasma modeling: Two-dimensional fluid-dynamics and propulsive performances," *Phys. Plasmas*, vol. 20, no. 4, p. 043512, Apr. 2013.

[26] J. M. Little and E. Y. Choueiri, "Thrust and efficiency model for electron-driven magnetic nozzles," *Phys. Plasmas*, vol. 20, no. 10, p. 103501, Oct. 2013.

[27] P. Chabert and N. Braithwaite, *Physics of Radio-Frequency Plasmas*. Cambridge, U.K.: Cambridge Univ. Press, 2011.

[28] K. Takahashi, C. Charles, and R. W. Boswell, "Approaching the theoretical limit of diamagnetic-induced momentum in a rapidly diverging magnetic nozzle," *Phys. Rev. Lett.*, vol. 110, no. 19, p. 195003, May 2013.

[29] M. D. West, C. Charles, and R. W. Boswell, "Operating radio frequency antennas immersed in vacuum: Implications for ground-testing plasma thrusters," *J. Propuls. Power*, vol. 26, no. 4, pp. 892–896, Jul./Aug. 2010.

[30] C. Charles, R. W. Boswell, and A. Bish, "Variable frequency matching to a radiofrequency source immersed in vacuum," *J. Phys. D, Appl. Phys.*, vol. 46, no. 36, p. 365203, Aug. 2013.

[31] I. D. Sudit and F. F. Chen, "RF compensated probes for high-density discharges," *Plasma Sources Sci. Technol.*, vol. 3, no. 2, p. 162, May 1994.

[32] P. M.-H. Chung, L. Talbot, and K. J. Touryan, *Electric Probes in Stationary and Flowing Plasmas: Theory and Application*. New York, NY, USA: Springer-Verlag, 1975.

[33] F. F. Chen, "Langmuir probe analysis for high density plasmas," *Phys. Plasmas*, vol. 8, no. 6, p. 3029, Feb. 2001.

[34] A. Smirnov, Y. Raitses, and N. J. Fisch, "Plasma measurements in a 100 W cylindrical hall thruster," *J. Appl. Phys.*, vol. 95, no. 5, pp. 2283–2292, Feb. 2004.

[35] A. Ellingboe and R. Boswell, "Capacitive, inductive and helicon-wave modes of operation of a helicon plasma source," *Phys. Plasmas*, vol. 3, no. 7, p. 2797, Apr. 1996.

[36] C. M. Franck, O. Grulke, and T. Klinger, "Mode transitions in helicon discharges," *Phys. Plasmas*, vol. 10, no. 1, pp. 323–325, Oct. 2002.

[37] T. Lafleur, C. Charles, and R. W. Boswell, "Electron temperature characterization and power balance in a low magnetic field helicon mode," *J. Phys. D, Appl. Phys.*, vol. 44, no. 18, p. 185204, Apr. 2011.

[38] A. Fruchtman, G. Makrinich, and J. Ashkenazy, "Two-dimensional equilibrium of a low temperature magnetized plasma," *Plasma Sources Sci. Technol.*, vol. 14, no. 1, p. 152, Feb. 2005.

[39] L. Liard, J.-L. Raimbault, and P. Chabert, "Competitive effects of an axial magnetic field and of neutral gas depletion in a positive column," *Phys. Plasmas*, vol. 16, no. 5, p. 053507, 2009.

[40] J. E. Stevens, M. J. Sowa, and L. M. Cecchi, "Helicon plasma source excited by a flat spiral coil," *J. Vac. Sci. Technol. A, Vac. Surf., Films*, vol. 13, no. 5, pp. 2476–2482, 1995.

[41] G. Sato, W. Oohara, and R. Hatakeyama, "Experimental characterization of a density peak at low magnetic fields in a helicon plasma source," *Plasma Sources Sci. Technol.*, vol. 16, no. 4, p. 734, Sep. 2007.

[42] T. Lafleur, C. Charles, and R. W. Boswell, "Ion beam formation in a very low magnetic field expanding helicon discharge," *Phys. Plasmas*, vol. 17, no. 4, p. 043505, Apr. 2010.

[43] T. Lafleur, C. Charles, and R. W. Boswell, "Plasma control by modification of helicon wave propagation in low magnetic fields," *Phys. Plasmas*, vol. 17, no. 7, p. 073508, Jul. 2010.

[44] T. Lafleur, C. Charles, and R. W. Boswell, "Characterization of a helicon plasma source in low diverging magnetic fields," *J. Phys. D, Appl. Phys.*, vol. 44, no. 5, p. 055202, Jan. 2011.

[45] T. Lafleur, C. Charles, and R. W. Boswell, "Electron-cyclotron damping of helicon waves in low diverging magnetic fields," *Phys. Plasmas*, vol. 18, no. 4, p. 043502, Apr. 2011.

[46] T. Lho, N. Hershkowitz, J. Miller, W. Steer, and G. H. Kim, "Azimuthally symmetric pseudosurface and helicon wave propagation in an inductively coupled plasma at low magnetic field," *Phys. Plasmas*, vol. 5, no. 9, p. 3135, May 1998.

[47] F. F. Chen, "Introduction to plasma physics and controlled fusion," *Plasma Phys.*, vol. 1, 2nd ed. New York, NY, USA: Springer-Verlag, 1984.

[48] E. Ahedo, "Parametric analysis of a magnetized cylindrical plasma," *Phys. Plasmas*, vol. 16, no. 11, p. 113503, Nov. 2009.

[49] H. Lorzel and P. G. Mikellides, "Three-dimensional modeling of magnetic nozzle processes," *AIAA J.*, vol. 48, no. 7, pp. 1494–1503, Jul. 2010.

[50] A. Fruchtman, "The thrust of a collisional plasma source," *IEEE Trans. Plasma Sci.*, vol. 39, no. 1, pp. 530–539, Jan. 2011.

Justin M. Little was born in Seattle, WA, USA, in 1984. He received the B.S. (*summa cum laude*) degree in aerospace engineering and physics from the University of California at Irvine, Irvine, CA, USA, in 2008, and the M.A. degree in mechanical and aerospace engineering from Princeton University, Princeton, NJ, USA, in 2010, where he is currently pursuing the Ph.D. degree with the Electric Propulsion and Plasma Dynamics Laboratory.

His current research interests include electric propulsion, RF plasmas, plasma-magnetic field interactions, and space plasma physics.

Mr. Little was the recipient of the National Defense Science and Engineering Graduate Fellowship in 2009. He is a member of the American Institute for Aeronautics and Astronautics and the Electric Rocket Propulsion Society.

Edgar Y. Choueiri received the Ph.D. degree from the Department of Mechanical and Aerospace, Princeton University, Princeton, NJ, USA, in 1991.

He is a Professor of Applied Physics with the Department of Mechanical and Aerospace, Princeton University, where he is also the Director of Electric Propulsion and Plasma Dynamics Laboratory, the 3-D Audio and Applied Acoustics Laboratory, and the Program in Engineering Physics. He has authored more than 175 publications on plasma propulsion, plasma physics, and space physics.

Prof. Choueiri served as a President of the Electric Rocket Society and Chair of the American Institute for Aeronautics and Astronautics's (AIAA) Electric Propulsion Technical Committee. He is a fellow of the AIAA and recipient of numerous prizes and awards.